



**HAL**  
open science

## Polarization effects in lattice–STED microscopy

Bin Yang, Fang C.-Y., Chang H.-C., François Treussart, Jean-Baptiste Trebbia, Brahim Lounis

► **To cite this version:**

Bin Yang, Fang C.-Y., Chang H.-C., François Treussart, Jean-Baptiste Trebbia, et al.. Polarization effects in lattice–STED microscopy. *Faraday Discussions*, 2015, 184, pp.37-49. 10.1039/C5FD00092K . hal-01359602

**HAL Id: hal-01359602**

**<https://hal.science/hal-01359602>**

Submitted on 2 Sep 2016

**HAL** is a multi-disciplinary open access archive for the deposit and dissemination of scientific research documents, whether they are published or not. The documents may come from teaching and research institutions in France or abroad, or from public or private research centers.

L'archive ouverte pluridisciplinaire **HAL**, est destinée au dépôt et à la diffusion de documents scientifiques de niveau recherche, publiés ou non, émanant des établissements d'enseignement et de recherche français ou étrangers, des laboratoires publics ou privés.

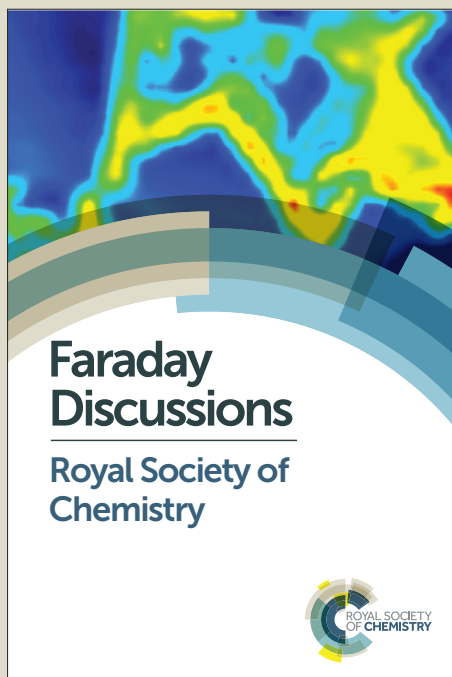
# Faraday Discussions

Accepted Manuscript



This manuscript will be presented and discussed at a forthcoming Faraday Discussion meeting. All delegates can contribute to the discussion which will be included in the final volume.

**Register now to attend!** Full details of all upcoming meetings: <http://rsc.li/fd-upcoming-meetings>



This is an *Accepted Manuscript*, which has been through the Royal Society of Chemistry peer review process and has been accepted for publication.

*Accepted Manuscripts* are published online shortly after acceptance, before technical editing, formatting and proof reading. Using this free service, authors can make their results available to the community, in citable form, before we publish the edited article. We will replace this *Accepted Manuscript* with the edited and formatted *Advance Article* as soon as it is available.

You can find more information about *Accepted Manuscripts* in the [Information for Authors](#).

Please note that technical editing may introduce minor changes to the text and/or graphics, which may alter content. The journal's standard [Terms & Conditions](#) and the [Ethical guidelines](#) still apply. In no event shall the Royal Society of Chemistry be held responsible for any errors or omissions in this *Accepted Manuscript* or any consequences arising from the use of any information it contains.

This article can be cited before page numbers have been issued, to do this please use: B. Yang, C. FANG, H. Chang, F. TREUSSART, J. Trebbia and B. Lounis, *Faraday Discuss.*, 2015, DOI: 10.1039/C5FD00092K.



## Journal Name

## ARTICLE

## Polarization Effects in Lattice-STED Microscopy

Received 00th January 20xx,

Accepted 00th January 20xx

DOI: 10.1039/x0xx00000x

[www.rsc.org/](http://www.rsc.org/)B. Yang<sup>a,b</sup>, C.-Y. Fang<sup>c</sup>, H.-C. Chang<sup>c</sup>, F. Treussart<sup>d</sup>, J.-B. Trebbia<sup>a,b</sup> and B. Lounis<sup>a,b</sup>

Massive parallelization of STED-like nanoscopies is now achievable using well-designed optical lattices for state depletion. Yet, only the lattice intensity distribution was considered for the description of the super-resolved point spread function. This holds for fast-rotating fluorescent emitters. Here, we study the effects of electric field topography in lattice-STED microscopy. The dependence of the super-resolved point spread function on the number of dipoles and their orientation is investigated. Single fluorescent nano-diamonds are imaged using different optical lattice configurations and the measured resolutions are compared to theoretical simulations.

## Introduction

Fluorescence images of emitters separated by less than half of the wavelength are not resolvable due to the diffraction limit. By surpassing this limit and providing resolution down to a few nanometers, super-resolution microscopy techniques<sup>1,2</sup> have revolutionized far-field optical microscopy in the last decade. These techniques exploit the photo-physical and photo-chemical properties of emitters to make them fluoresce sequentially and therefore to optically resolve them. The sequential selective imaging is achieved either in stochastic or deterministic ways. Stochastic super-resolution methods are based on the localization of isolated single emitters<sup>3-9</sup>. Deterministic methods<sup>10-15</sup>, such as stimulated emission depletion (STED)<sup>10</sup> are based on patterned laser illuminations, which restrict the fluorescence emission to pre-determined nanoscale regions. This sequential imaging modality implies that the resolution gain is at the expense of the imaging speed, which could be a severe limitation when studying dynamic structures in living cells, since many biological phenomena occur at timescales from milliseconds to seconds<sup>16,17</sup>. Although localization-based methods are intrinsically parallelized, their imaging speeds are limited by the density of the fluorescent emitters per raw image and by the stochastic process of emitters on/off switching. The acquisition time of a super-resolved image usually lays in the range of 1-100 s<sup>2,18-20</sup>.

<sup>a</sup> Univ Bordeaux, LP2N, F-33405 Talence, France.<sup>b</sup> Institut d'Optique & CNRS, LP2N, F-33405 Talence, France.<sup>c</sup> Institute of Atomic and Molecular Sciences, Academia Sinica, Taipei 106, Taiwan.<sup>d</sup> Laboratoire Aimé Cotton, UMR 9188 CNRS, ENS Cachan and Université Paris Sud, 91405 Orsay, France.

DOI: 10.1039/x0xx00000x

Standard STED microscopy is a point-scanning technique<sup>21</sup> which requires only a limited number of fluorescence photons integrated over dwell times down to several tens of  $\mu\text{s}$ <sup>22</sup>, to obtain the local density of emitters. However, the imaging speed of large fields of view is however strongly limited since dense pixelization is required.

An important step towards massive parallelization of STED-like nanoscopies has been achieved using well-designed optical lattices for state depletion<sup>23, 24</sup>. These lattices contain an array of unit cells, each of which has a point-like intensity minimum surrounded by a nearly isotropic intensity distribution. Combined with a homogeneous wide-field illumination for fluorescence excitation, each unit cell plays the same role as a doughnut beam of confocal STED, which reduces the fluorescence emission volume to a sub-diffraction scale by stimulated emission depletion. To obtain a super-resolution image, one only needs to scan the sample over a unit cell of the optical lattice rather than the entire field of view. With this Lattice-STED approach, imaging of  $3\ \mu\text{m} \times 3\ \mu\text{m}$  field of view with a resolution of 70 nm and a speed of 80 ms per super-resolution image has been achieved<sup>23</sup>. The low pulse energy of the high repetition rate laser used for the depletion and the readout time of the camera set the limit of the field of view and the imaging speed, respectively. Using a laser with lower repetition rate and higher pulse energy, larger fields of view can be imaged<sup>25</sup>.

In the aforementioned experiments, the polarization effects in the depletion lattice have been neglected. Only the lattice intensity distribution was considered for the description of the super-resolved point spread function (s-PSF). This description holds for fast-rotating fluorescent emitters with rotation characteristic time much shorter than the depletion pulse for which the polarization effects are averaged. In this paper, we study the effects of electric field topography in lattice-STED microscopy. The dependence of the s-PSF on the number of dipoles and their orientations is investigated. Single nano-diamonds containing a few Nitrogen-Vacancy (NV) fluorescent defects are imaged using different optical lattice configurations and the measured s-PSF are compared to theoretical simulations.

### Optical lattices

Optical lattices are periodic patterns generated by multi-beam interferences. They were first introduced in cold atoms trapping and manipulation<sup>26-28</sup>. Their applications have been extended to other fields such as photonic crystal fabrication<sup>29</sup> and microfluidics<sup>30</sup>. The electric field topology (i.e. spatial distributions of its amplitude and its polarization) of an optical lattice depends on the number of interfering beams, their directions, polarizations and relative phases<sup>27, 31</sup>.

The total electric field  $\vec{E}(\vec{r}, t)$  created by the interference of a number  $p$  of plane waves having the same amplitude  $\mathcal{E}$  writes:

$$\vec{E}(\vec{r}, t) = \sum_{j=1}^p \mathcal{E} e^{i(\vec{k}_j \cdot \vec{r} - \omega t + \phi_j)} \vec{e}_j = \mathcal{E} e^{i(\vec{k}_p \cdot \vec{r} - \omega t + \phi_p)} \left( \vec{e}_p + \sum_{j=1}^{p-1} e^{i((\vec{k}_j - \vec{k}_p) \cdot \vec{r} + \phi_j - \phi_p)} \vec{e}_j \right) \quad (1)$$

Where  $\vec{k}_j$ ,  $\omega$ ,  $\phi_j$ ,  $\vec{e}_j$  are respectively the wave vector, the angular frequency, the phase and the polarization directions of each plane wave. The vector position  $\vec{r}$  has  $q$  spatial coordinates corresponding to the space dimension  $q$ . Since the arbitrary choice of the time origin allows cancelling the phases  $\phi_p$ , the number of independent relative phases in Equation (1) is  $(p - 1)$ . Furthermore, the arbitrary choice of the space origin ( $\vec{r} = \vec{r}' + \vec{r}_0$ ) allows rewriting the spatial dependence of the electric field as:

$$\vec{E}(\vec{r}) = \mathcal{E} \left( \vec{e}_p + \sum_{j=1}^{p-1} e^{i(\vec{k}_j - \vec{k}_p) \cdot \vec{r}'} e^{i((\vec{k}_j - \vec{k}_p) \cdot \vec{r}_0 + \phi_j - \phi_p)} \vec{e}_j \right) \quad (2)$$

This equation clearly shows that any relative phase variation between the beams results in a global spatial translation of the optical lattice ( $\vec{r}_0$ , without any change in the field topography) if the system of  $(p - 1)$  linear equations of  $q$  variables ( $(\phi_j - \phi_p + (\vec{k}_j - \vec{k}_p) \cdot \vec{r}_0) = 0$ ,  $1 \leq j \leq p - 1$ ) has a solution<sup>31</sup>. For independent wave vectors, this requirement is fulfilled if the number of interfering beams  $p$  is equal to  $q + 1$ .

In the case of 2D imaging ( $q = 2$ ), the interference of three beams will lead to an optical lattice which keeps both the topographies of the electric field and of the intensity independent of the beams phases. A four-beam optical lattice has an electric field topography that depends on the beams relative phases. However, in certain configurations, the intensity topography is insensitive to the beams phases and leads to better STED parallelization.

### Three beam configuration

To build a three-beam optical lattice in the focal plane of a microscope objective suitable for STED parallelization, we consider three beams propagating in the direction of the optical axis of the objective ( $\vec{e}_z$ ) with the same linear polarization ( $\vec{e}_x$ ), as shown in Fig. 1a. The beams intersect the objective at the vertices of a centered equilateral triangle. After passing through the objective they are deviated by an angle  $\theta$  toward the focal region where they interfere and form an optical lattice. The incident beams are slightly focused Gaussian beams with beam waists located at the back focal plane of the objective. The transmitted beams are collimated and deviated by the objective and have their polarizations rotated. The interference of the three beams leads to a lattice with hexagonal structures with a periodicity of  $\frac{2\lambda}{3n \sin(\theta)}$ ,  $n$  being the refractive index of the medium and  $\lambda = 760$  nm the depletion wavelength. Optical lattices useful for STED nanoscopy (local zero-intensity minima, each of which surrounded by nearly isotropic intensity distribution) can be obtained when the three incident beams have their

polarizations parallel to one of the three sides of the incidence triangle shown in Fig. 1a. Fig. 1b shows the intensity distribution of the optical lattices obtained for an incidence angle  $\theta = 72^\circ$ . At this angle, the hexagonal pattern displays a period of 355 nm and an optimal intensity contrast, better than 99.9%. The intensity profiles along two directions in the x-y plane (blue and green lines in Fig. 1c) are identical up to 150 nm away from the zero intensity position. Such depletion intensity profile should lead to an almost isotropic s-PSF when imaging fast rotating emitters.

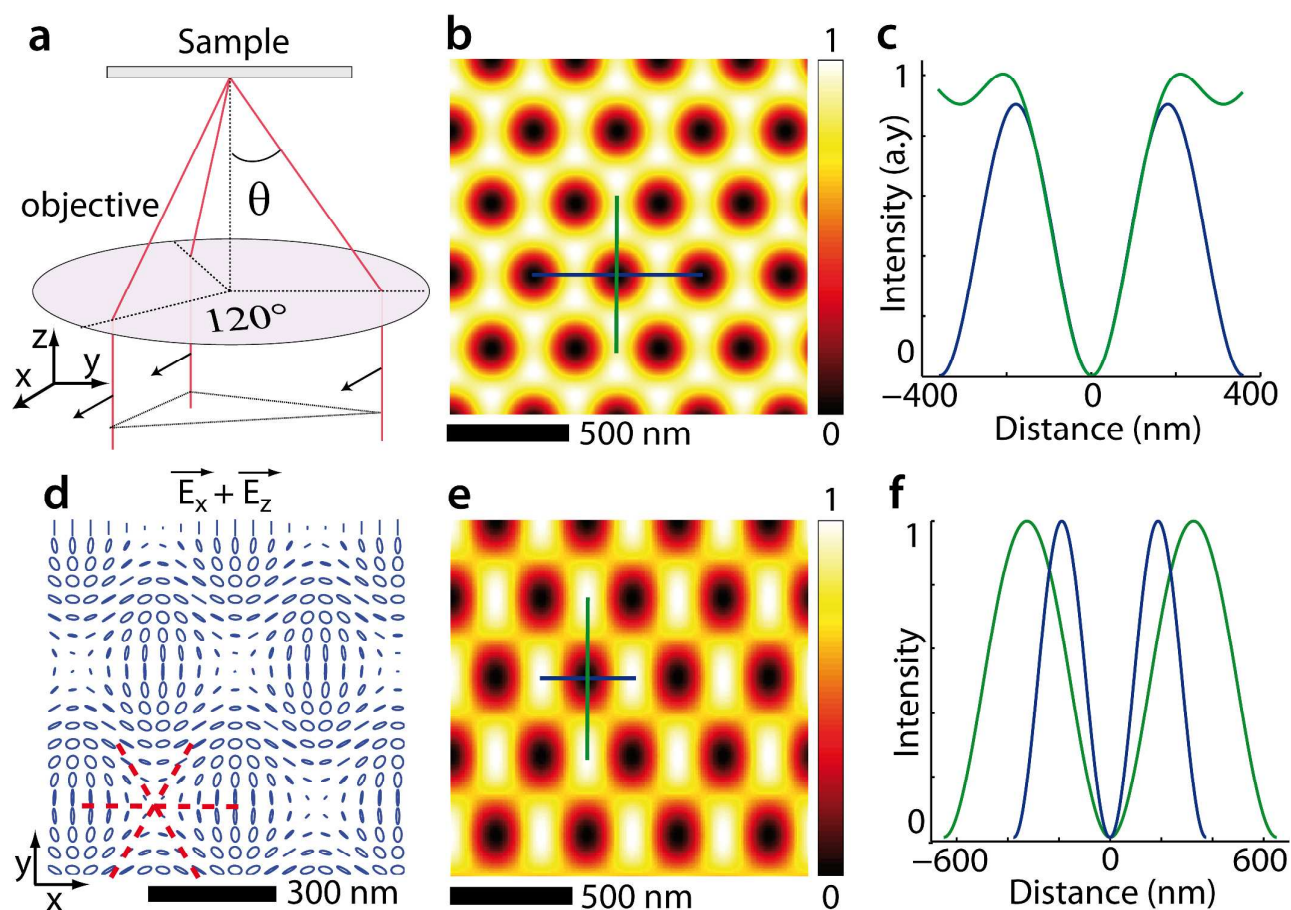


**Fig. 1** a) Three beam configuration. b) Resulting intensity topography of the interference pattern for  $\theta = 72^\circ$ . c) Cross sectional intensity plots along the blue and green lines of b). d) Electric field topography for  $\theta = 72^\circ$ . Only the electric field polarization in the plane (x,z) is plotted. Straight lines, ellipses and circles indicate respectively linear, elliptical and circular polarizations. Red dashed lines correspond to the directions where the electric field is linear. e)-f) Resulting intensity topography and the associated cross sectional intensity plots.

In the imaging plane (x,y), the amplitudes of the electric field projections along the x and z directions are significantly larger than that along y direction since the incident beams have the same polarization ( $\vec{e}_x$ ). The polarization topography of the electric field projection in the (x,z) plane is shown in Fig. 1d. Around the intensity

minima, the polarization is elliptical except along the three directions shown by the red dashed lines in Fig. 1d where it is linear. As discussed above, the field topography is insensitive to any phase variations of the incident beams.

In practice, the back aperture of the objective and the size of the beams at this aperture limit the maximum achievable incidence angle. In the experiment, we use an oil immersion objective (N.A. = 1.49, back aperture diameter  $\sim 10$  mm) which allows to achieve an angle  $\theta = 60^\circ$  with beam diameters of 1 mm. In this case, the optical pattern shown in Fig. 1e still displays "zero-intensity" regions with a contrast close to unity (98%). However, as shown in the intensity profiles of Fig. 1f, the intensity gradient around the locations of the zeros is steeper in the horizontal direction.

### Four beam configuration

A key point for faster Lattice-STED imaging is to generate lattices with the smallest possible unit cell. For this purpose, we use a four-beam interference configuration where a smaller unit cell can be obtained with the same angle  $\theta$ . If one uses two orthogonally polarized pairs of beams (Fig. 2a), each pair will generate a one-dimensional interference pattern independently from the other pair of beams. The intensity distribution of the final optical lattice is just the sum of the two one-dimensional interference patterns and a square optical lattice with a periodicity  $\frac{\lambda}{2n\sin(\theta)} = 290$  nm can be obtained for  $\theta = 60^\circ$  and  $\lambda = 760$  nm, as shown in Fig. 2b.

Fig. 2c shows the intensity plots along the x-axis (green) and the diagonal direction (blue). The maximal intensity along the diagonal direction is twice that along the x-axis. Nevertheless the intensity gradients around the intensity "zeros" are very similar. Therefore the resolution should be almost isotropic when imaging fast-rotating molecules. The intensity topography of the lattice (Fig. 2b) is insensitive to the relative phase between the beams. The electric field in the imaging plane is:

$$\vec{E}(x, y) = 2\mathcal{E} \left[ \sin\left(\frac{2\pi n}{\lambda}(x - x_0)\sin(\theta)\right) \vec{e}_x + \sin\left(\frac{2\pi n}{\lambda}(y - y_0)\sin(\theta)\right) e^{i\Delta\phi} \vec{e}_y \right] \quad (3)$$

where  $x_0$  and  $y_0$  are the 2D spatial coordinate of  $\vec{r}_0$  and  $\Delta\phi$  is the relative phase between the two orthogonal standing waves. The electric field topography only depends on  $\Delta\phi$  and it is depicted in Fig. 2d-2f. For  $\Delta\phi = 0$ , the polarization of the field is linear everywhere in the imaging plane. If  $\Delta\phi \neq 0$ , the polarization around the zero intensity regions is linear only along the x and y axis, while it is elliptical anywhere else. It becomes circular along the directions  $\pm 45^\circ$  when  $\Delta\phi = \pi/2$ .

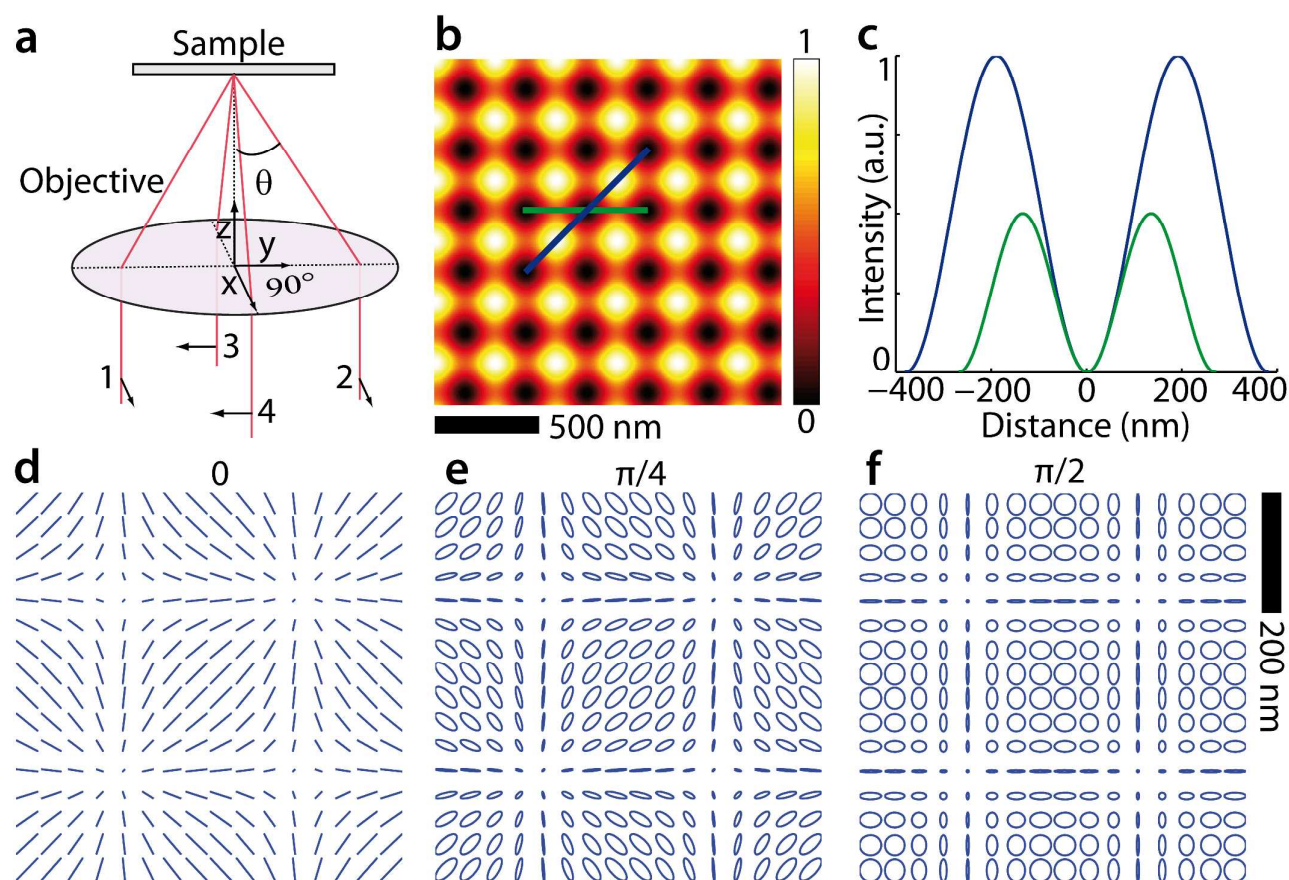


**Fig 2** a) Geometrical four beams configuration. b) Resulting intensity topography of the interference pattern for  $\theta = 60^\circ$ . c) Cross sectional intensity plots along the blue and green lines of b). d)-f) plots of the electric field polarization in the plane (x,y) for  $\Delta\phi = 0, \frac{\pi}{4}, \frac{\pi}{2}$ . Straight lines, ellipses and circles indicate respectively linear, elliptical and circular polarizations.

### Influence of the polarization pattern on lattice-STED s-PSF

Fluorescent emitters commonly used in STED have a 1D transition dipole moment. Their excited state depletion efficiency depends on the squared projection of the electric field on the direction of their dipole moment. Rotating molecules have a time dependent orientation of their dipole  $\vec{d} = d \vec{e}_d(t)$  and a characteristic rotational time  $T_{rot}$ . The intensity relevant in the interaction of this dipole with the field  $\vec{E}$  is the effective local intensity  $I_{eff} = \langle |\vec{e}_d(t) \cdot \vec{E}(\vec{r})|^2 \rangle$ , averaged over the integration time.

To model the lattice-STED s-PSF, we construct a fluorescence emission image obtained when an ensemble of emitters localized in a nanoscale region (such as an ensemble of molecules in a nanosphere or a bunch of NV centers in a nano-diamond) are scanned in the focal plane of the objective in presence of a homogeneous wide-field excitation illumination and a depletion optical lattice. In this case, the fluorescence signal can usually be well

approximated by the expression  $S_{fluor} \sim e^{-\left(\frac{\ln(2)I_{eff}}{I_{sat}}\right)}$ , where  $I_{sat}$  is the saturation intensity which is defined as the intensity at which the probability of fluorescence intensity is reduced by half<sup>21, 32</sup>. The image provides information about the depletion pattern (structure and periodicity). The spatial regions where the fluorescence is not depleted give directly access to the expected s-PSF.

Three different rotational mobility regimes should be considered: the first regime, introduced above, is the fast-rotation regime where  $T_{rot}$  is much shorter than the duration of the depletion pulse. The second one corresponds to the intermediate situation where the molecules display a slow rotational diffusion, characterized by  $T_{rot}$  much longer than the pulse duration and much shorter than the integration time. The last one is the regime of “fixed” molecules, obtained when  $T_{rot}$  is much longer than the integration time.

In the fast rotation regime, the transition dipole moment of the emitters can be considered as isotropic and the effective intensity profile is simply the intensity distribution of the depletion lattice. Time averaging over all possible orientations of the dipole during each depletion pulse results in a decrease of the intensity by an overall factor of 3. Therefore, the fluorescence signal can be depleted to zero in all directions around a zero intensity region. The images in Fig. 3a present the results of such simulations. The emitting dipoles are scanned over a region slightly larger than the unit cell of the optical lattice described above ( $\theta = 60^\circ$ , intensity maxima of  $6I_{sat}$ ). In the case of three-beam hexagonal lattice (left image) the s-PSF is elongated reflecting directly the anisotropy of the intensity distribution of Fig. 1e-f. For the four-beams square lattice, the s-PSF is isotropic and does not depend on the relative phase difference  $\Delta\phi$  between the two orthogonal standing waves (as shown in the images constructed for  $\Delta\phi = 0, \frac{\pi}{4}$  and  $\frac{\pi}{2}$ ).

In the two other regimes, the polarization pattern of the electric field has to be taken into account since dipoles perpendicular to the field polarization are not depleted, even at high STED intensities. Images of a small number of emitters exhibiting slow rotational diffusion or of a bead containing a large number of fixed emitters can be modeled in the same way. The fluorescence signal is calculated by averaging the fluorescence contributions of a large number of dipoles randomly oriented in a three-dimensional space:

$$S_{fluor} \sim \sum_{i=1}^N e^{-\left(\frac{\ln(2)I_{eff}^i}{I_{sat}}\right)} \quad (4)$$

where  $I_{eff}^i$  is the effective field intensity which depletes the excited dipole  $\vec{d}_i$ . The results of a calculation performed with  $N = 500$  dipoles are shown in Fig. 3b. The fluorescence images display strong correlations with the polarization patterns of Fig. 1d and Fig. 2d-f. For example, in the three beam configuration, the fluorescence image shows that from each zero-intensity region (corresponding to a fluorescence maximum in the image) there

are three directions where the fluorescence is not efficiently depleted. They correspond to that presented in Fig. 1d giving the directions along which the lattice field is linearly polarized. An interesting situation is obtained in the four-beam configuration when  $\Delta\phi = 0$ . Since the electric field polarization is linear everywhere, excited emitters are not depleted where their dipole moments are perpendicular to the local field during the scan. Therefore the fluorescence signal cannot be decreased to zero even at higher STED intensities. For  $\Delta\phi = \frac{\pi}{2}$ , the emitters are efficiently depleted in the diagonal directions where the polarization of the field is close to circular. They cannot be completely depleted along the horizontal and vertical directions, where the polarization of the field is linear.

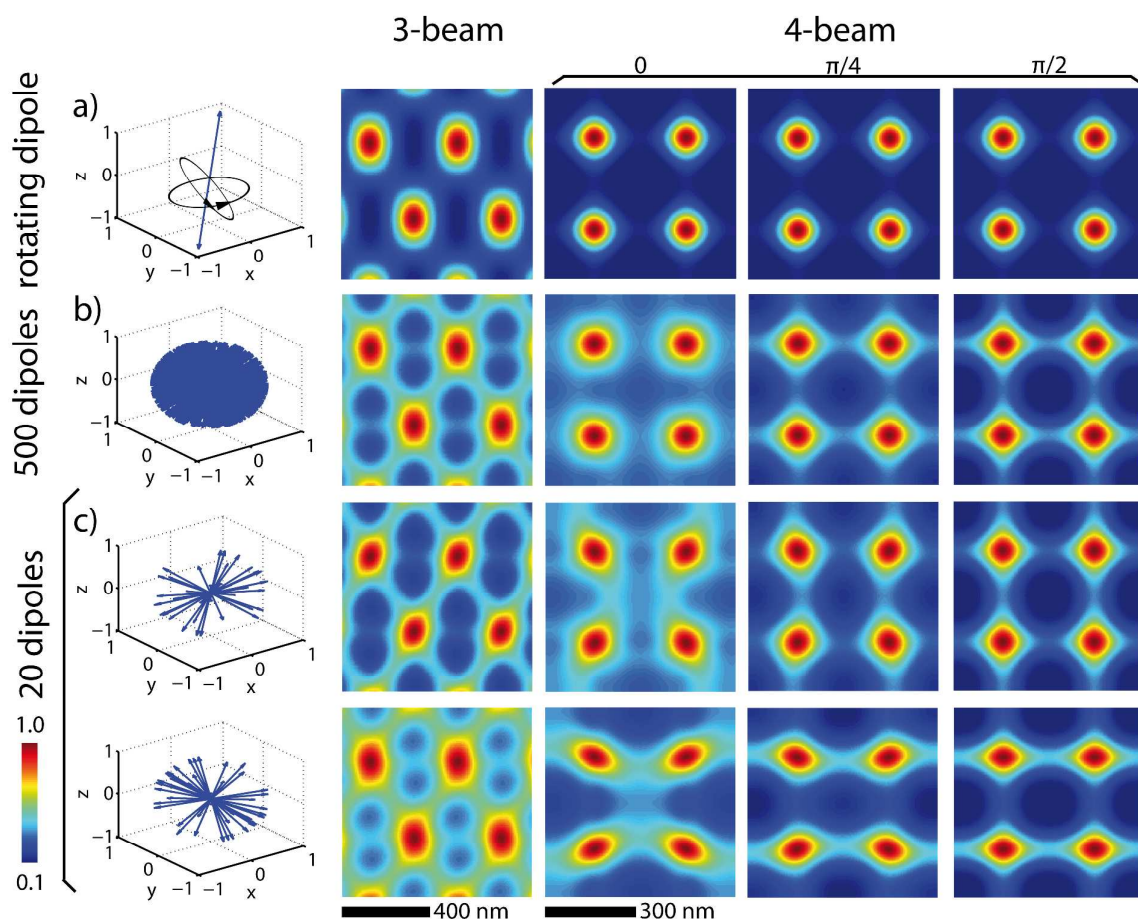


**Fig. 3** Simulated fluorescence depletion patterns obtained for different dipole orientations in the three and the four beams optical lattices and for different  $\Delta\phi$  ( $0, \frac{\pi}{4}, \frac{\pi}{2}$ ) in the cases of : a fast 3D rotating dipole (a), a large number of randomly oriented dipole directions (500) (b), and two different sets of 20 randomly oriented dipoles (3D) (c) at a depletion intensity of  $I = 6I_{\text{sat}}$ .

Polarization effects are more pronounced when the localized emission stems from a small number of fixed molecules. In this case, the s-PSF depends strongly on the orientation of dipoles as shown in Fig. 3c. The images are calculated for two configurations of 20 randomly oriented dipoles. In the four beam lattice, the shape of the s-PSF varies also strongly with the lattice relative phase  $\Delta\phi$ . The optimal configuration, which gives the most symmetric s-PSF is obtained for  $\Delta\phi=\pi/2$ .

## Experimental Setup

Our Lattice-STED microscopy setup, sketched in Fig. 4a, is based on two synchronized laser sources delivering excitation and depletion pulses, akin to a standard STED microscope<sup>32</sup>. The fluorescence excitation beam (wavelength 571 nm and pulse duration 2 ps) is delivered by a frequency doubled optical parametric oscillator (Mira-OPO, Coherent) pumped by picosecond Ti-sapphire laser (Mira 900 Coherent) at a repetition rate of 76 MHz. A second Ti-sapphire active mode-locked laser (Tsunami, Spectra Physics) emitting at 760 nm, provides the depletion beam. It is synchronized with the excitation laser and delivers Fourier transform limited pulses of ~100 ps duration at an average power of 2.5 W. A Spatial Light Modulator or a set of two Wollaston prisms, conjugated with the sample plane, is used to generate multiple depletion beams (Fig. 4b). The laser beams are focused on the back focal plane of a high numerical aperture objective and illuminate a wide-field region of the sample (~7.5  $\mu\text{m}$  x 7.5  $\mu\text{m}$ ). The optical lattice produced by interference of the depletion beams at the sample plane is superimposed on a uniform excitation beam. The fluorescence emission is collected with the same objective, filtered from excitation and depletion photons and sent to a fast CMOS camera (ORCA-Flash4.0, HAMAMATSU). A fast piezo-scanner is used for sample scanning.

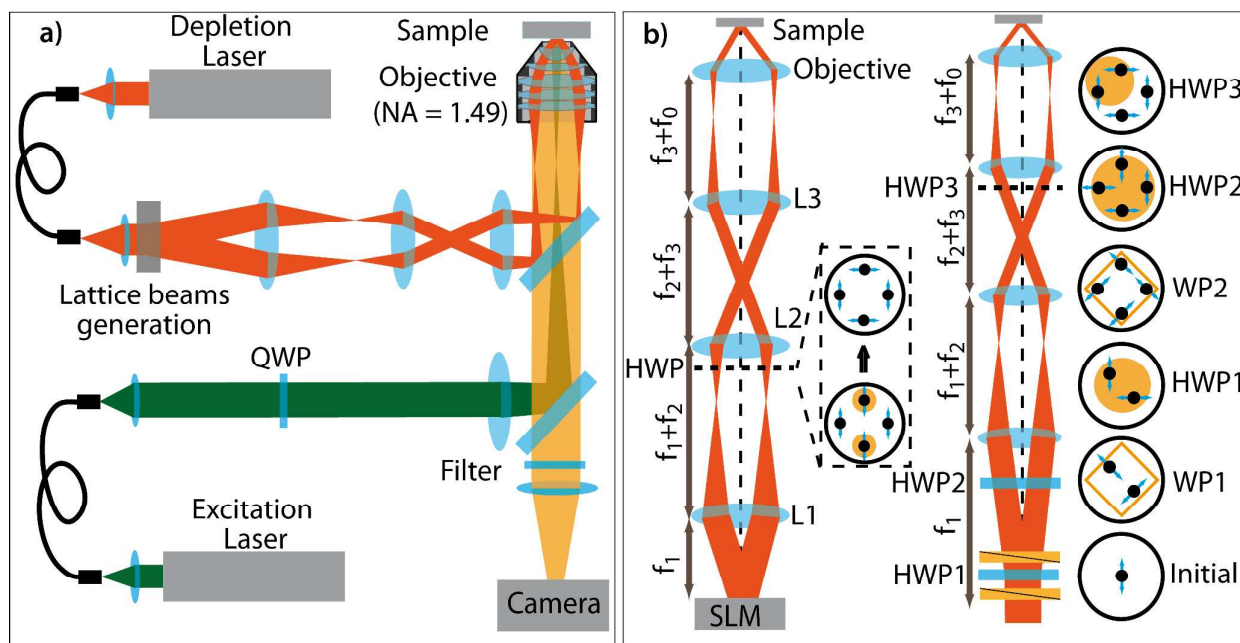


**Fig. 4** a) Optical setup of the Lattice-STED microscope. The depletion beams are sent through an objective and interfere at the sample plane to form a 2D optical lattice. This optical pattern is superimposed on a wide-field excitation beam ( $\sim 10 \mu\text{m} \times 10 \mu\text{m}$ ). A CMOS camera conjugated with the sample plane records the wide-field fluorescence images. The lattice generator is either a Spatial Light Modulator (SLM) or a set of two Wollaston prisms. It is conjugated with the sample plane by a set of 3 lenses (L1, L2 and L3) and the objective, with focal lengths  $f_1$ ,  $f_2$ ,  $f_3$  and  $f_0$ , as shown in b) for both configurations. Black spots illustrate the intersections of the beams with the different planes, blue double arrows show the polarizations. Orange circles and squares indicate respectively the half-wave plates (HWP) and the Wollaston prisms.

The left scheme of Fig. 4b shows the generation of the multi-beam optical lattice with the SLM. The SLM surface is conjugated with the sample plane by three lenses and the objective. The focal lengths of the lenses are carefully chosen to set both the desired angle of incidence and size of the optical lattice at the sample plane. The size of the optical lattice is determined by the available STED laser power and the desired resolution. For the hexagonal lattice configuration, the SLM produces three beams with the same polarization. For the square lattice, the four beams diffracted by the SLM initially have the same linear polarization. Two half-wave plates are used to obtain two beam pairs of orthogonal polarization. The diffraction efficiency of 4-beam generation with the SLM being only 40%, we can use two Wollaston prisms (WP) to generate the four beams so as to minimize power losses (right scheme of Fig. 4b). Starting from a linear vertical polarization, a first Wollaston prism splits the beam into two beams, with orthogonal polarizations  $\pm 45^\circ$ . A half-wave plate (HWP1) rotates the polarization of the two beams into vertical and horizontal. A second Wollaston prism further splits the two beams into four. At last, two half-wave plates (HWP2 and HWP3) together set the polarizations of the four beams as in Fig. 2a. Depending on

the chosen system, the phase difference  $\Delta\phi$  could be adjusted either with the SLM hologram pattern or by the use of a tilted glass plate inserted in the beam paths.

The sample is composed of a thin layer of fluorescent nano-diamonds (size 35 nm) spin-coated on a glass coverslip. The number of NV defect centers per nano-diamond is  $\sim 15^{33}$ . The emission from individual nano-diamonds shows an extreme photo-stability. The amplitude of the signal, which varies from a nano-diamond to another, can be used for a rough estimation of the number of emitting defects contained in the nanoparticle.

## Experimental Results

Fig. 5a-5b represent a fluorescence image obtained by scanning a single nano-diamond with a piezo-stage over the field of illumination in presence of both depletion and excitation beams, while recording its fluorescence with the CMOS camera. For each scanning step (15 nm), an image is acquired and the fluorescence intensity, integrated over the image spot of the tracked nano-diamond on the camera, is plotted. The signal maxima of the images correspond to the regions of minimal depletion, which occur at the zero-intensity positions of the optical lattice. As expected for the case of three interfering beams with an incidence angle  $\theta = 60^\circ$ , we observed a hexagonal pattern with a periodicity of 390 nm. A field of view exceeding  $6 \mu\text{m} \times 6 \mu\text{m}$  can be achieved. The zoomed image shows that the s-PSF is elongated with an aspect ratio of  $\sim 2$ . Directions along which the depletion is not efficient are in agreement with the simulation of Fig. 3b for a large ensemble of emitting dipoles. Indeed, this nano-diamond was chosen among those presenting the highest fluorescence emission signal, i.e. those presenting a large number of NV defects. Using a total depletion average power of 850 mW an s-SPSF of 80 nm could be achieved.

Lattice-STED super-resolved images has been acquired following the procedure described in reference<sup>23</sup>. The sample containing fluorescent nano-diamonds is scanned over a unit cell of the depletion lattice in the presence of the wide field excitation and the depletion pattern, while acquiring a fluorescence image for each scanning step with the s-CMOS camera. We then overlay a binary mask on these images which acts as an array of parallelized "point detectors". The complete Lattice-STED image is then obtained by assembling the entire unit cell images together obtained for each "point detector".

Fig. 5c and 5d display  $5.7 \mu\text{m} \times 5.7 \mu\text{m}$  images of a sample containing fluorescent nano-diamonds spin-coated on a glass coverslip without and with the depletion pattern, respectively. Fig. 5c clearly shows that the PSF of the nano-diamonds are diffraction limited  $\sim 290 \text{ nm}$ , while the resolution of the Lattice-STED image of Fig. 5d is well below this limit (typically  $\sim 80 \text{ nm}$ ).

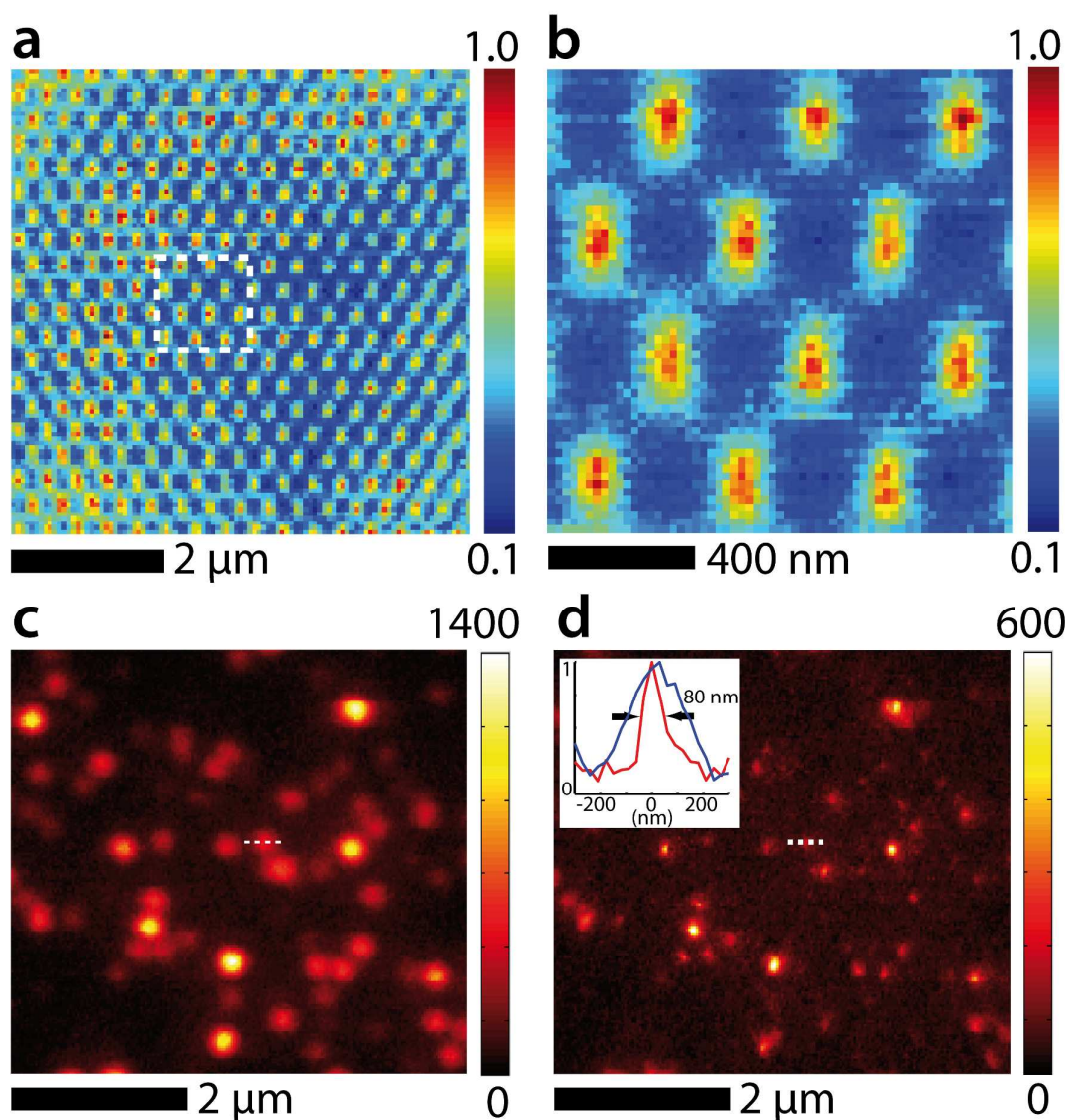


**Fig. 5** a) Experimental depletion patterns. Field of view:  $6 \mu\text{m} \times 6 \mu\text{m}$  recorded at an excitation power of 16 mW, and a depletion power of 850 mW (measured before the objective). Integration time per pixel: 20 ms. b) Zoom of the central region (white dashed square). All images are normalized with respect to their maximal intensities. c) and d) Three-beam Lattice-STEDED images of a sample containing 35 nm fluorescent nano-diamonds without and with the depletion optical lattice respectively. Field of view:  $5.7 \mu\text{m} \times 5.7 \mu\text{m}$ . pixel size: 30 nm, pixel dwell time: 20 ms. Inset: intensity profiles of a single nano-diamond (white dashed line) which shows a FWHM of 80 nm. Images obtained with the same excitation and depletion intensities. The scale bar corresponds to counts per unit of pixel dwell time.

The results with the four-beam square lattice are presented in Fig. 6. Fig. 6a-6c are constructed using the same procedure as in Fig. 5b. Depletion patterns obtained at three different values of  $\Delta\phi$  ( $0$ ,  $\frac{\pi}{4}$  and  $\frac{\pi}{2}$ ) are studied, and images recorded with three different weakly emitting nano-diamonds are shown. Using the total emission of the nanoparticle we can estimate the number of NV centers to a few tens. As predicted in Fig. 3, the shape of the s-

PSF strongly changes from one nano-diamond to another. The s-PSF is not always symmetric but depends on the relative phase  $\Delta\phi$  of the lattice, as expected.

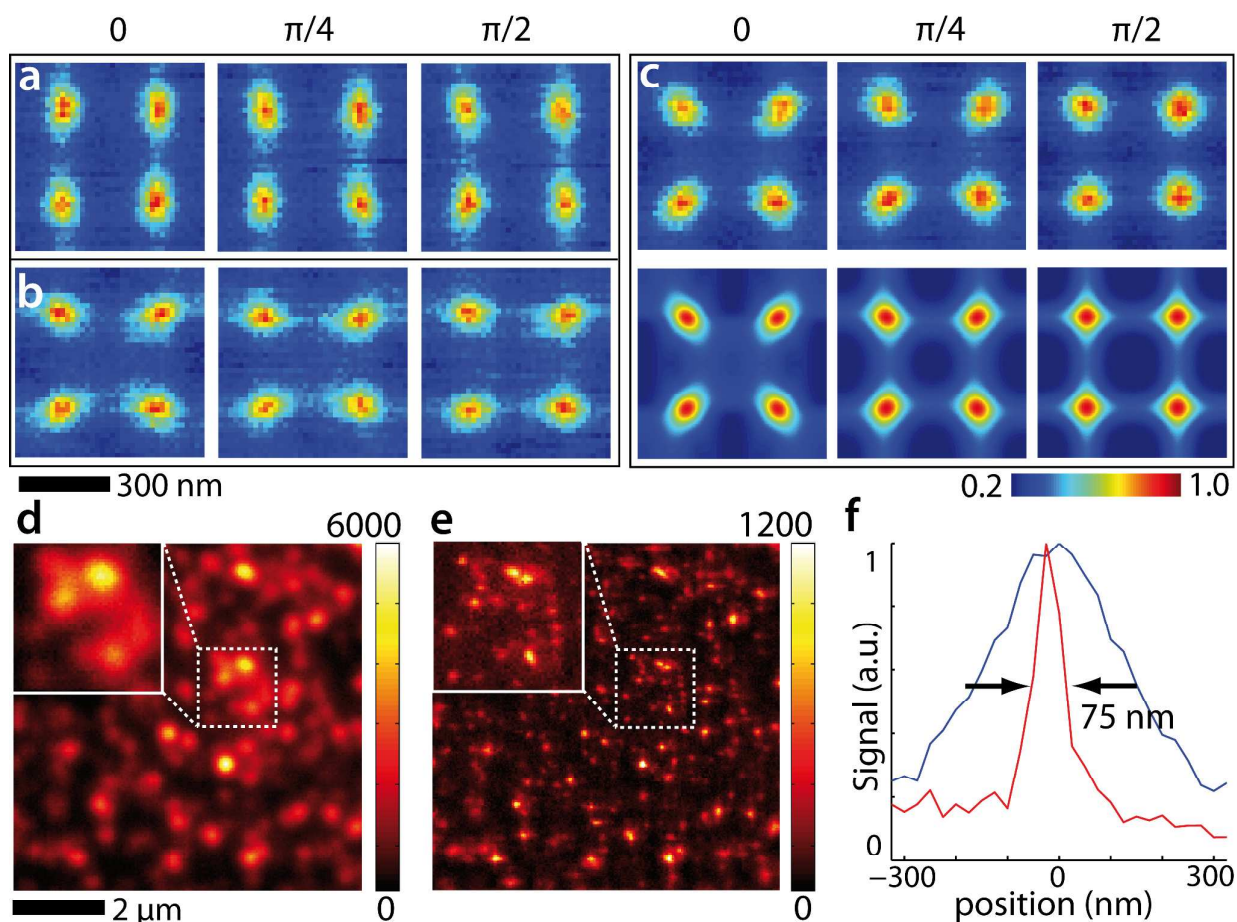


Fig. 6 a), b) and c) Experimental fluorescence depletion patterns measured for  $\Delta\phi=0, \pi/4$  and  $\pi/2$ . d) Simulated image computed with a set of twenty randomly oriented emitters depleted at an intensity maxima of  $6I_s$ . This simulation reproduces well the experimental s-PSF of image c). Integration time per pixel : 20 ms. All images are normalized with respect to their maximal intensities. e) and f) Four-beam Lattice-STED images of a sample containing 35 nm fluorescent nano-diamonds without and with the depletion optical lattice, respectively. Field of view : 7.5  $\mu\text{m}$  x 7.5  $\mu\text{m}$ . Pixel size : 30 nm, pixel dwell time : 20 ms. g) Intensity profile of a single nano-diamond with a FWHM of 75 nm. Images obtained with an excitation power of 16 mW and a depletion power of 850 mW measured before the objective.

For  $\Delta\phi = 0$  (field pattern of Fig. 2d), the s-PSFs are elongated, indicating a preferential orientation of emitting dipoles. In each image, the variations of the s-PSF orientation from site to site are imposed by the local

## ARTICLE

View Article Online  
DOI: 10.1039/C5FD00092K

polarization distribution around the zero intensity regions: the s-PSFs are elongated along the direction where the electric field is perpendicular to the dipoles average orientation. For example, the nano-diamond used in Fig. 6c has dipoles preferentially oriented along a diagonal direction. The images could be reproduced (Fig. 6d) with a set of twenty random emitters (having a diagonal average orientation) using the depletion lattices of Fig. 2 with intensity maxima of  $6I_{sat}$ . As  $\Delta\phi$  increases up to  $\pi/2$ , the anisotropy of the s-PSF gets less pronounced. The configuration for which  $\Delta\phi = \pi/2$  is therefore the most favorable to perform four-beam Lattice-STED microscopy.

As for the three beams configuration, we acquire Lattice-STED super-resolved images of a dense sample of nano-diamonds for  $\Delta\phi = \pi/2$ . Fig. 6e and 6f display  $7.5 \mu\text{m} \times 7.5 \mu\text{m}$  images without and with the four beams depletion pattern. A clear resolution improvement between these two images is visible. The s-PSF shown in Fig. 6g ( $\sim 75\text{nm}$ ) is well below the diffraction limit. Compared to the three beams configuration, the lattice unit cell is smaller and the intensity gradients around the zero-intensity regions are steeper, enabling a larger field of view with the same averaged depletion power.

### Conclusions

In this paper, we push further the investigations and the performance of Lattice-STED which massively parallelizes STED microscopy. Super-resolution images of 75 nm resolution and a field view of  $7.5 \mu\text{m} * 7.5 \mu\text{m}$  could be achieved with moderate powers of a high repetition rate laser. Images of fluorescent nano-diamonds acquired using different optical lattices configurations are compared to theoretical simulations. The results show that the s-PSF of Lattice-STED varies with the electric field topography of the lattices and should depend to the rotational diffusion properties of the emitters. This allowed finding the optimum configuration of four-beam lattice-STED nanoscopy.

### Acknowledgements

We warmly thank Philippe Tamarat for careful reading of the manuscript. We acknowledge financial support from the Agence Nationale de la Recherche, Région Aquitaine, the French Ministry of Education and Research, the European Research Council and FranceBioImaging (Grant N° ANR-10-INSB-04-01).

### Notes and references

1. B. Huang, M. Bates and X. Zhuang, *Annual review of biochemistry*, 2009, **78**, 993-1016.
2. A. G. Godin, B. Lounis and L. Cognet, *Biophysical journal*, 2014, **107**, 1777-1784.
3. E. Betzig, G. H. Patterson, R. Sougrat, O. W. Lindwasser, S. Olenych, J. S. Bonifacino, M. W. Davidson, J. Lippincott-Schwartz and H. F. Hess, *Science*, 2006, **313**, 1642-1645.
4. M. J. Rust, M. Bates and X. Zhuang, *Nature methods*, 2006, **3**, 793-795.
5. M. Heilemann, S. van de Linde, M. Schüttelz, R. Kasper, B. Seefeldt, A. Mukherjee, P. Tinnefeld and M. Sauer, *Angewandte Chemie International Edition*, 2008, **47**, 6172-6176.

6. A. Sharonov and R. M. Hochstrasser, *Proceedings of the National Academy of Sciences*, 2006, **103**, 18911-18916.
7. G. Giannone, E. Hosy, F. Levet, A. Constals, K. Schulze, Alexander I. Sobolevsky, M. P. Rosconi, E. Gouaux, R. Tampé, D. Choquet and L. Cagnet, *Biophysical Journal*, **99**, 1303-1310.
8. B. Huang, W. Wang, M. Bates and X. Zhuang, *Science*, 2008, **319**, 810-813.
9. J. Folling, M. Bossi, H. Bock, R. Medda, C. A. Wurm, B. Hein, S. Jakobs, C. Eggeling and S. W. Hell, *Nature methods*, 2008, **5**, 943-945.
10. S. W. Hell and J. Wichmann, *Opt. Lett.*, 1994, **19**, 780-782.
11. S. W. Hell and M. Kroug, *Appl. Phys. B*, 1995, **60**, 495-497.
12. M. G. Gustafsson, *J Microsc*, 2000, **198**, 82-87.
13. R. Heintzmann, T. M. Jovin and C. Cremer, *J. Opt. Soc. Am. A*, 2002, **19**, 1599-1609.
14. M. G. L. Gustafsson, *Proceedings of the National Academy of Sciences of the United States of America*, 2005, **102**, 13081-13086.
15. E. H. Rego, L. Shao, J. J. Macklin, L. Winoto, G. A. Johansson, N. Kamps-Hughes, M. W. Davidson and M. G. L. Gustafsson, *Proceedings of the National Academy of Sciences*, 2012, **109**, E135-E143.
16. F. Huang, T. M. P. Hartwich, F. E. Rivera-Molina, Y. Lin, W. C. Duim, J. J. Long, P. D. Uchil, J. R. Myers, M. A. Baird, W. Mothes, M. W. Davidson, D. Toomre and J. Bewersdorf, *Nat Meth*, 2013, **10**, 653-658.
17. P. Kner, B. B. Chhun, E. R. Griffis, L. Winoto and M. G. L. Gustafsson, *Nat Meth*, 2009, **6**, 339-342.
18. S. A. Jones, S.-H. Shim, J. He and X. Zhuang, *Nat Meth*, 2011, **8**, 499-505.
19. L. Zhu, W. Zhang, D. Elnatan and B. Huang, *Nat Meth*, 2012, **9**, 721-723.
20. J. Huang, M. Sun, K. Gumpfer, Y. Chi and J. Ma, *Biomed Opt Express*, 2015, **6**, 902-917.
21. S. W. Hell, *Nature biotechnology*, 2003, **21**, 1347-1355.
22. V. Westphal, S. O. Rizzoli, M. A. Lauterbach, D. Kamin, R. Jahn and S. W. Hell, *Science*, 2008, **320**, 246-249.
23. B. Yang, F. Przybilla, M. Mestre, J.-B. Trebbia and B. Lounis, *Opt. Express*, 2014, **22**, 5581-5589.
24. A. Chmyrov, J. Keller, T. Grotjohann, M. Ratz, E. d'Este, S. Jakobs, C. Eggeling and S. W. Hell, *Nat Methods*, 2013, **10**, 737-740.
25. P. Bingen, M. Reuss, J. Engelhardt and S. W. Hell, *Opt. Express*, 2011, **19**, 23716-23726.
26. A. Hemmerich and T. W. Hänsch, *Physical Review Letters*, 1993, **70**, 410-413.
27. G. Grynberg, B. Lounis, P. Verkerk, J. Y. Courtois and C. Salomon, *Physical Review Letters*, 1993, **70**, 2249-2252.
28. M. Greiner, O. Mandel, T. Esslinger, T. W. Hansch and I. Bloch, *Nature*, 2002, **415**, 39-44.
29. M. Campbell, D. N. Sharp, M. T. Harrison, R. G. Denning and A. J. Turberfield, *Nature*, 2000, **404**, 53-56.
30. M. P. MacDonald, G. C. Spalding and K. Dholakia, *Nature*, 2003, **426**, 421-424.
31. B. Lounis, PhD thesis, Université Paris Sud - Paris XI, 1993.
32. B. Harke, J. Keller, C. K. Ullal, V. Westphal, A. Schönle and S. W. Hell, *Optics Express*, 2008, **16**, 4154-4162.
33. C.-C. Fu, H.-Y. Lee, K. Chen, T.-S. Lim, H.-Y. Wu, P.-K. Lin, P.-K. Wei, P.-H. Tsao, H.-C. Chang and W. Fann, *Proceedings of the National Academy of Sciences*, 2007, **104**, 727-732.